Mineralization of sulfide mound at Wocan-1 hydrothermal field based on geological mapping, mineralogy and sulfur isotope studies, Carlsberg Ridge, Northwest Indian Ocean

Yiyang Cai [a,b], Xiqiu Han [a,b,*], Sven Petersen [c], Yejian Wang [b,*], Zhongyan Qiu [b], Ming Yang [a,b]

[a] *School of Oceanography, Shanghai Jiao Tong University, Shanghai 200030, China*
[b] *Key Laboratory of Submarine Geosciences & Second Institute of Oceanography, Ministry of Natural Resources, Hangzhou 310012, China*
[c] *GEOMAR, Helmholtz Centre for Ocean Research Kiel, Kiel 24148, Germany*

ABSTRACT

The Wocan-1 hydrothermal field is distinct on the occurrence of an active sulfide mound, discovered on an axial volcanic ridge of the slow-spreading Carlsberg Ridge. The size of the mound is comparable to TAG active mound located in off-axis of Mid-Atlantic Ridge. In order to understand its formation and controlling factors, we did field geological mapping, mineralogical and geochemical analysis on the hydrothermal precipitates. Our results show the sulfide mound is $\sim$ 260 m in diameter and $\sim$ 50 m in height. The southern area of the mound is enriched in high-temperature Cu-rich sulfides, while the northern area is characterized by moderate-temperature Fe-rich sulfides and a talus of pyrite-anhydrite breccias and sands extending for > 200 m. The pyrite here exhibits recrystallization textures characterized by heavier δ^{34}S compositions when compared to that in the southern area. It is considered that the normal faults extending into the northern area of the mound and the associated mass wasting facilitated the infiltration of seawater, which is responsible for the regional difference in mineralization of the mound. This study contributes to the understanding of the formation and controls of large sulfide mounds on the AVRs at the slow-spreading ridges.

1. Introduction

Seafloor massive sulfides are often seen as one possible source for metals to maintain future supply needs (Hannington et al., 2005). Since the first discovery of massive sulfides on the East Pacific Rise in 1978, more than 400 sulfide-bearing hydrothermal fields have been identified in various tectonic settings (Hannington et al. 2023; Teagle and Alt, 2004; Cherkashov et al., 2017; Pelleter et al., 2017). Among them, the slow-spreading mid-ocean ridges are one of the most important environments for the formation of hydrothermal deposits (Hannington et al., 2011). A number of deposits with resources potential have been identified in off-axis settings, for example, TAG and Rainbow on the Mid-Atlantic Ridge (Rona et al., 1986; Fouquet et al., 1997), Yuhuang and Longqi along the Southwest Indian Ridge (Tao et al., 2011; Yu et al., 2021) and Tianxiu on the Carlsberg Ridge (Du et al., 2023). Seafloor massive sulfides also form in axial environments of slow-spreading ridges, such as axial volcanic ridges (AVRs). Typical cases, including Snake Pit, Broken Spur, Tongguan and Deyin hydrothermal fields, are usually characterized by the presence of individual chimneys with no or small sulfide mounds (Fouquet et al., 1993; Butler et al., 1998; Wang et al., 2016; Wang et al., 2022). However, there are a few exceptional cases such as Beebe (Webber et al., 2015) and Loki's Castle (Pedersen et al., 2010) from ultra-slow spreading ridges, and Wocan-1 from slow-spreading Carlsberg Ridge (Wang et al., 2017; Qiu et al., 2021), these fields all have relatively large hydrothermal mound in the size over 100 m.

Wocan-1 is a high-temperature hydrothermal field discovered in 2013 during the Chinese DY 28th cruise (Wang et al., 2017). Previous studies have investigated the sulfides, sediments, plume and hydrothermal circulation in the Wocan-1 field. Both high-temperature and lower-temperature mineralization has been reported in this area (Wang et al., 2017). The hydrothermal activity at Wocan-1 has lasted at least 1070 years, with the oldest age of massive sulfide samples dated by U-Th chronology yielding 10.6 ka (Qiu et al. 2021). Numerical simulation study indicates the depth and maximum temperature of potential heat sources within the Wocan-1 are approximately 1 km and T_{max} = 550 $^{\circ}$C,
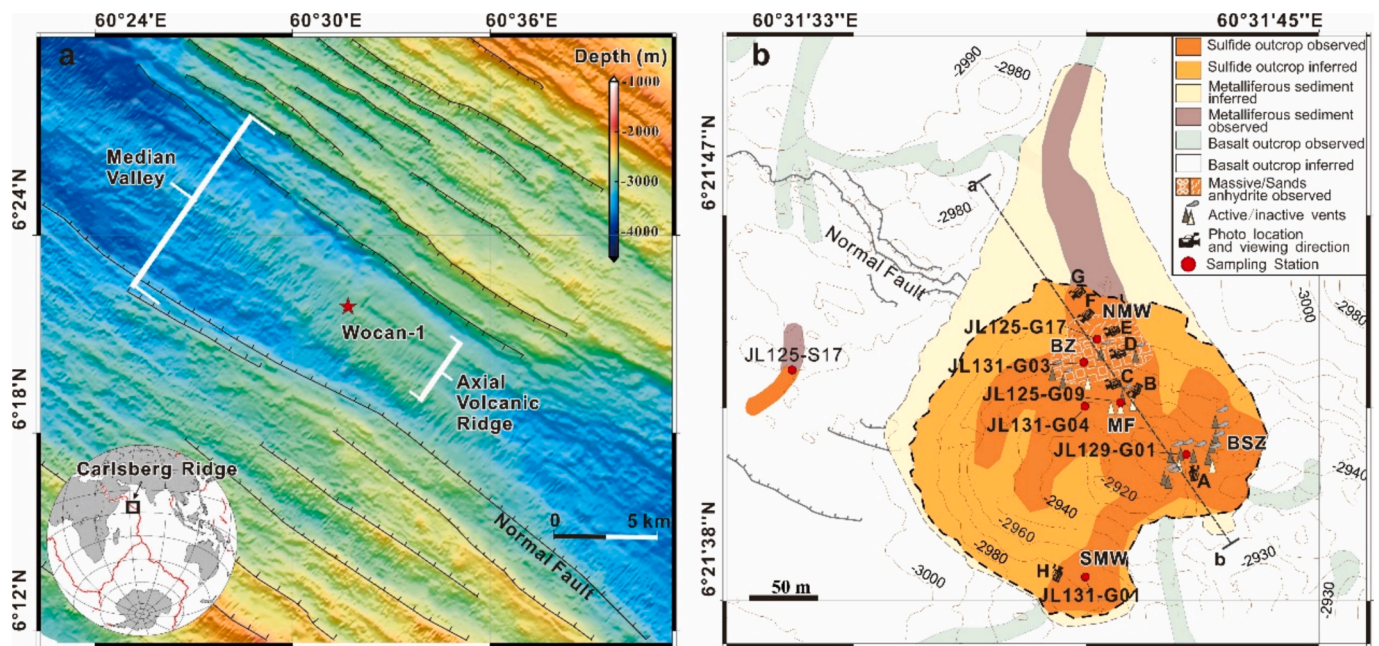
Fig. 1. Bathymetric map of the survey area over Carlsberg Ridge and geological map of the Wocan-1 active mound. a The figure is modified after Wang et al. (2017) and the location of the active Wocan-1 hydrothermal field. b The figure is modified after Qiu et al. (2021). Interpreted from the high-resolution bathymetry, surface samples, and video surveys. The JL125-S17 is the short sediment core station previously reported by Qiu et al. (2021). A~H labelled the locations of the corresponding images shown in Fig. 2. Abbreviations: BSZ- Black Smoker Zone, MF- Mulberry Forest, BZ- Beehive Zone, SMW- Southern Mass Wasting, NMW- Northern Mass Wasting.

Table 1
The characteristics of various areas of Wocan-1 mound.

Zone	Location	Water Depth (m)	Topography	Activity	Hydrothermal Deposit	Mineralogy
Black Smoker Zone (BSZ)	Summit and southeast slope of mound	2920 ~ 2960	Steep deposits	Focused vents with black smoke. Max. T=358℃	Torch and pipe like chimney, massive sulfides	Major: Ccp, Sph, Py, Mar Minor: Cv, Opal
Mulberry Forest (MF)	~70 m on the northwest of BSZ	2950 ~ 2960	Gentle slope	Focused vents with clear fluid	Organ pipe chimneys	Major: Ccp, Sph, Py, Mar Minor: Bn, Dg, Cv, Opal-CT, Fe-oxyhydroxides
Beehive Zone (BZ)	~110 m on the northwest of BSZ	2970 ~ 2980	Gentle slope	Mainly diffuse flow, rarely focused vents Max. T=117℃	Beehive chimney, massive sulfides/ sulfates	Major: Py and Anh Minor: Ccp and Bn
Northern Mass Wasting (NMW)	Northern margin of the mound	2980 ~ 3008	Gentle slope		Massive pyrite/ anhydrite, Hydrothermal sediments	Major: Py and Anh
Southern Mass Wasting (SMW)	Southern margin of the mound	2955 ~ 2975	Gentle slope		Massive sulfides, Hydrothermal sediments	Major: Ccp, Sph, Py, Mar Minor: Cv, Opal-CT, Ata, Fe-oxyhydroxides

Note: Py- pyrite, Mrc- marcasite, Sph- sphalerite, Ccp- chalcopyrite, Bn- Bornite, Dg- Digenite, Cv- Covellite, Anh-anhydrite, Ata- atacamite.

respectively (Zeng et al. 2024). Yet, so far, the distribution of sulfides, the mineralization process and their controls remain unclear. In this study, we did geological mapping and detailed analysis of the mineralogy and sulfur isotopic composition of sulfides, with aim to reveal the distribution and features of the sulfide precipitates and their controlling factors at Wocan-1.

2. Geological background

The Carlsberg Ridge, which separates the Indian and Somalia tectonic plates in the northwest Indian Ocean, is a slow-spreading ridge with a full spreading rate of 22 ~ 32 mm/yr (Raju et al. 2008). It lies between Owen Fracture Zone and Li Daoyuan Fracture Zone, with a total length of ~ 1400 km (Raju et al. 2008; Yu et al. 2019). A number of hydrothermal fields with sulfide minerals have been discovered along the Carlsberg Ridge, including Tianxiu, Daxi, Wocan-1 and Wocan-2 (Han et al. 2015; Du et al., 2023; Wang et al. 2017; Wang et al., 2021a).

The Wocan ridge is a NW-SE oriented AVR located in the median valley of a symmetrical-spreading ridge segment of Carlsberg ridge (Fig. 1a; Wang et al. 2017). It extends for ~ 28 km and is 5.5 km wide in the middle and narrows at both ends, covering an area of about 220 km² (Fig. 1a; Wang et al. 2017). The Wocan-1 field, hosted by basalts, is located on the northwestern slope of the Wocan ridge at 6°21′ N, 60°31′ E, in a water depth of 2920 ~ 3120 m (Wang et al. 2017; Zong et al., 2019; Qiu et al. 2021).

3. Methods

3.1. Geological mapping and sampling

The bathymetric and side scan sonar data were obtained by bathymetric side-scan sonar (HRBSSS) system of the manned submersible *Jiaolong*. Underwater acoustic communication devices transmitted positioning data obtained by a POSIDONIA USBL on the supporting ship,
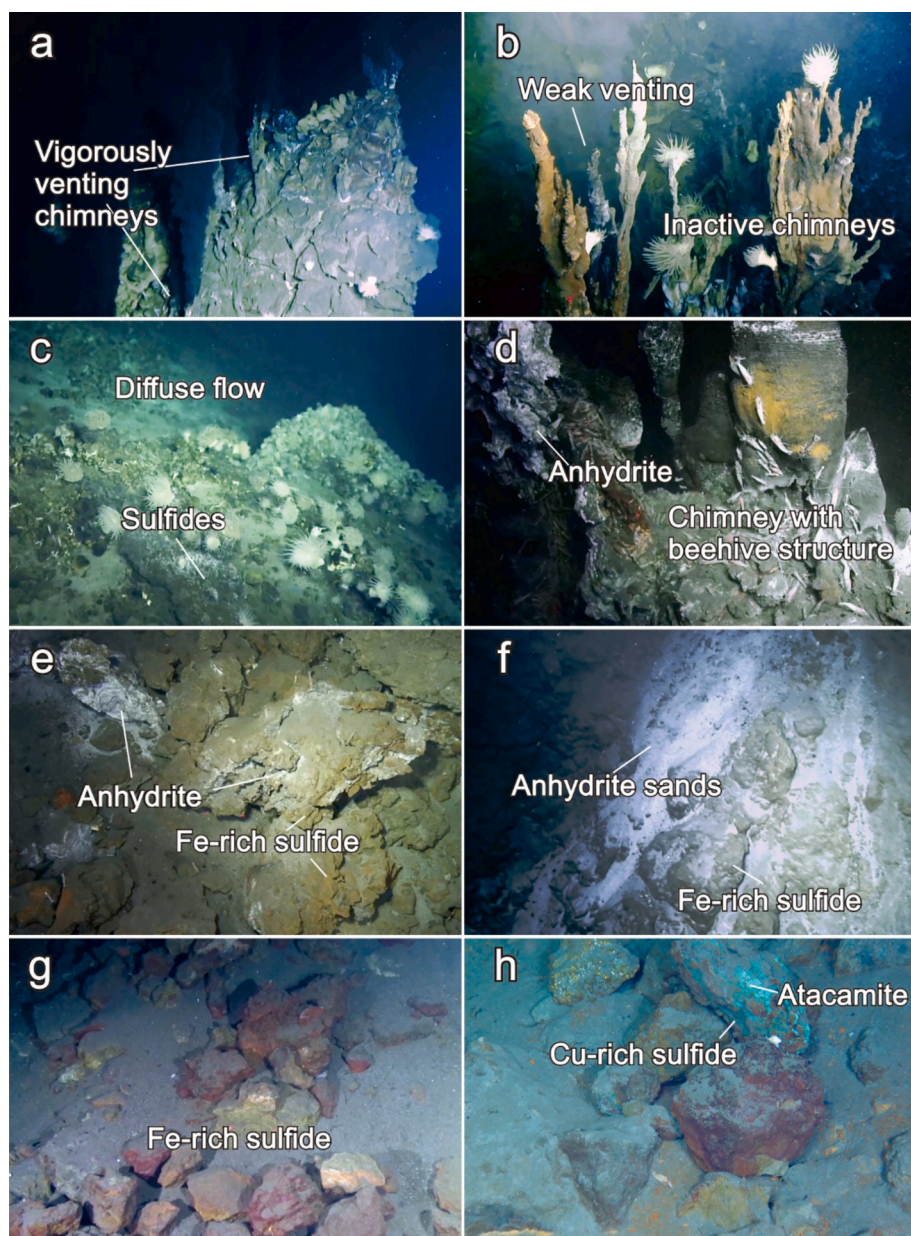
Fig. 2. Images of seafloor observation on the Wocan-1 mound. The locations of each image are shown in Fig. 1b. **a** Vigorously venting black smoker complex, field of view ~ 5 m. **b** Organ pipe chimneys with weak venting, field of view ~ 3 m. **c** Diffuse flow on the mound slope field of view ~ 5 m. **d** Chimneys with beehive structure emanating diffuse flow, field of view ~ 2 m. **e** Anhydrite and Fe-rich sulfides, field of view ~ 1 m. **f** Anhydrite sand on the northern slope of the mound, field of view ~ 5 m. **g** Mass wasting on the northern slopes of the mound, showing abundant Fe-rich sulfide, some have been oxidized into reddish iron-(hyro)oxides, field of view ~ 2 m. **h** Mass wasting on the southern slopes of the mound, showing abundant Cu-rich sulfide as indicated by the presence of atacamite, field of view ~ 1 m.

allowing for the determination of the initial position of the integrated navigation system (Zhang et al. 2018). The photograph was obtained by the optical system mounted on the submersible, which includes a 3 CCD TV (charged coupled device television) camera with parallel laser scale (0.1 m spacing), two 1CCD TV cameras, a pan-and-tilt digital still camera, and eight lights (Wang et al., 2021b). A series of geological and faunal samples were collected using the manipulator of the submersible.

3.2. Mineralogy and in-situ sulfur isotope analysis

We selected representative sulfide chimneys and breccias samples from six sampling stations. Each sample was photographed, sectioned, polished and described. Textural interpretations and mineral identifications were based on polished thin sections and X-ray diffraction (XRD) analyses at the Second Institute of Oceanography, Ministry of Natural

Resources, Hangzhou, China. Thin sections were examined under an optical microscope (Leica DM 2700P) using reflected and transmitted light. The XRD analyses were performed using an X'Pert PRO diffractometer with CuKα radiation generated at 45 kV and 40 mA. The databases utilized for XRD determinations are the Powder Diffraction File (PDF) and Inorganic Crystal Structure Database (ICSD).

Before conducting in situ sulfur isotope analyses, the samples were pretreated with NaOCl to reveal the internal zonations to ensure that no alteration and visible micro-inclusions. In situ sulfur isotope analyses of sulfides were performed by two methods. Chemical laser-ablation spot-analyzes on sulfide minerals were performed on a Neptune Plus MC-ICP-MS (Thermo Fisher Scientific, Bremen, Germany) equipped with a Geolas HD excimer ArF laser ablation system (Coherent, Göttingen, Germany) at the Wuhan SampleSolution Analytical Technology Co., Ltd, Hubei, China using the technique described by Hu et al. (2015) and Fu
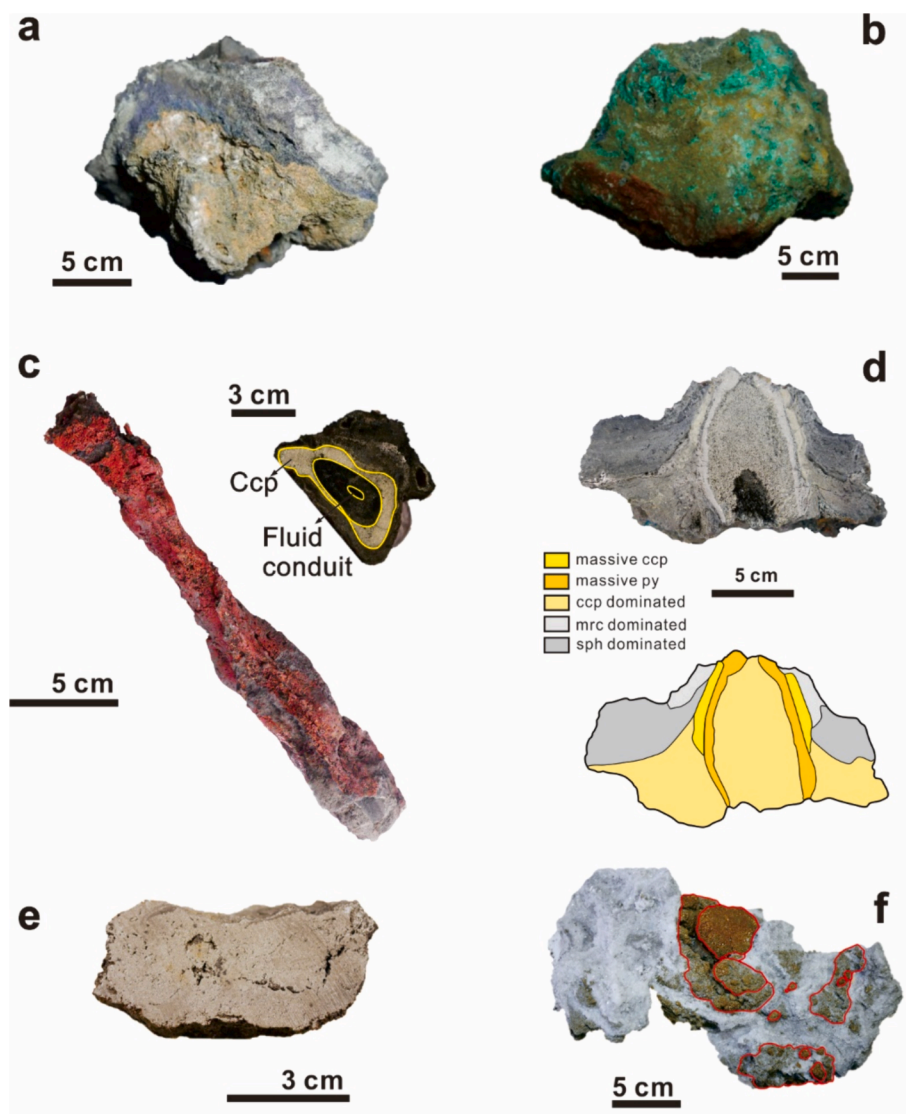
Fig. 3. Representative samples from the Wocan-1 mound. **a** Cu- rich chimney fragment collected from BSZ (sample JL129-G01). **b** Cu- rich chimney fragment collected from SMW, with typical greenish atacamite formed on the surface of the sample (sample JL131-G01). **c** An oxidized inactive organ pipe chimney (sample JL125-G09). The cross section of the sample shows its inner layer consists mainly of chalcopyrite (Ccp). **d** The vertical section and the sketch of a Cu-rich chimney collected in the vicinity of MF (sample JL131-G04), it shows multiple layers including two dense layers of pyrite (Py) and chalcopyrite (Ccp) respectively. **e** A massive pyrite sample collected from BZ (sample JL131-G03). **f** Yellowish matrix supported anhydrite-pyrite breccias collected from NMW (sample JL125-G17).

Table 2
The abundances of minerals in the samples collected from various areas of Wocan-1 mound.

Area	Sample ID	Type	Ccp	Sph	Py	Mar	Anh	Bn	Dg	Cv	Gn	Ba	Opal-CT	Ata	Fe-oxides
SMW	JL131-G01	Cu-rich chimney	+++	++	+	tr				tr			tr	+	tr
BSZ	JL129-G01	Cu-rich chimney	++	++	++	++				tr			+		
MF	JL125-G09	Cu-rich chimney	+++	++	+	+		+	tr	tr					+
MF	JL131-G04	Cu-rich chimney	++	++	++	++		tr		tr	tr	+	+		
BF	JL131-G03	Fe-rich massive sulfide	tr		+++										
NMW	JL125-G17	Massive anhydrite	+		++		+++								

Note: +++ Major (>50 %), ++Abundant (10–50 %), + Minor (1–10 %), tr-Trace (<1%).
Py- pyrite, Mrc- marcasite, Sph- sphalerite, Ccp- chalcopyrite, Bn- Bornite, Dg- Digenite, Cv- Covellite, Anh-anhydrite, Ata- atacamite.

et al. (2016). A spot size of 44 μm was used on pyrite and marcasite. The spot-to-spot reproducibility (external precision) was 0.2 ~ 0.4 ‰. A standard-sample bracketing method was employed to correct for instrumental mass fractionation. A pyrite standard PPP-1 was chosen as reference materials for correcting the natural pyrite and marcasite samples with values of $\delta^{34}S_{V-CDT}$ have been reported by Fu et al. (2016). The in-house references of a pyrrhotite SP-Po-01 ($\delta^{34}S_{V-CDT}$=1.4 ± 0.4 ‰) were analyzed repeatedly to verify the accuracy of the calibration method. Ion-probe analyses were performed by the Sensitive High-Resolution Ion MicroProbe SI (SHRIMP-SI) at Research School of Earth Sciences (RSES), Australian National University, using the technique described by Ireland et al. (2014). The secondary ion mass spectrometry measurement utilized a beam depth of ~ 1 μm and spot sizes of ~ 35 μm for pyrite and marcasite. Pyrite sulfur isotope data were normalized to
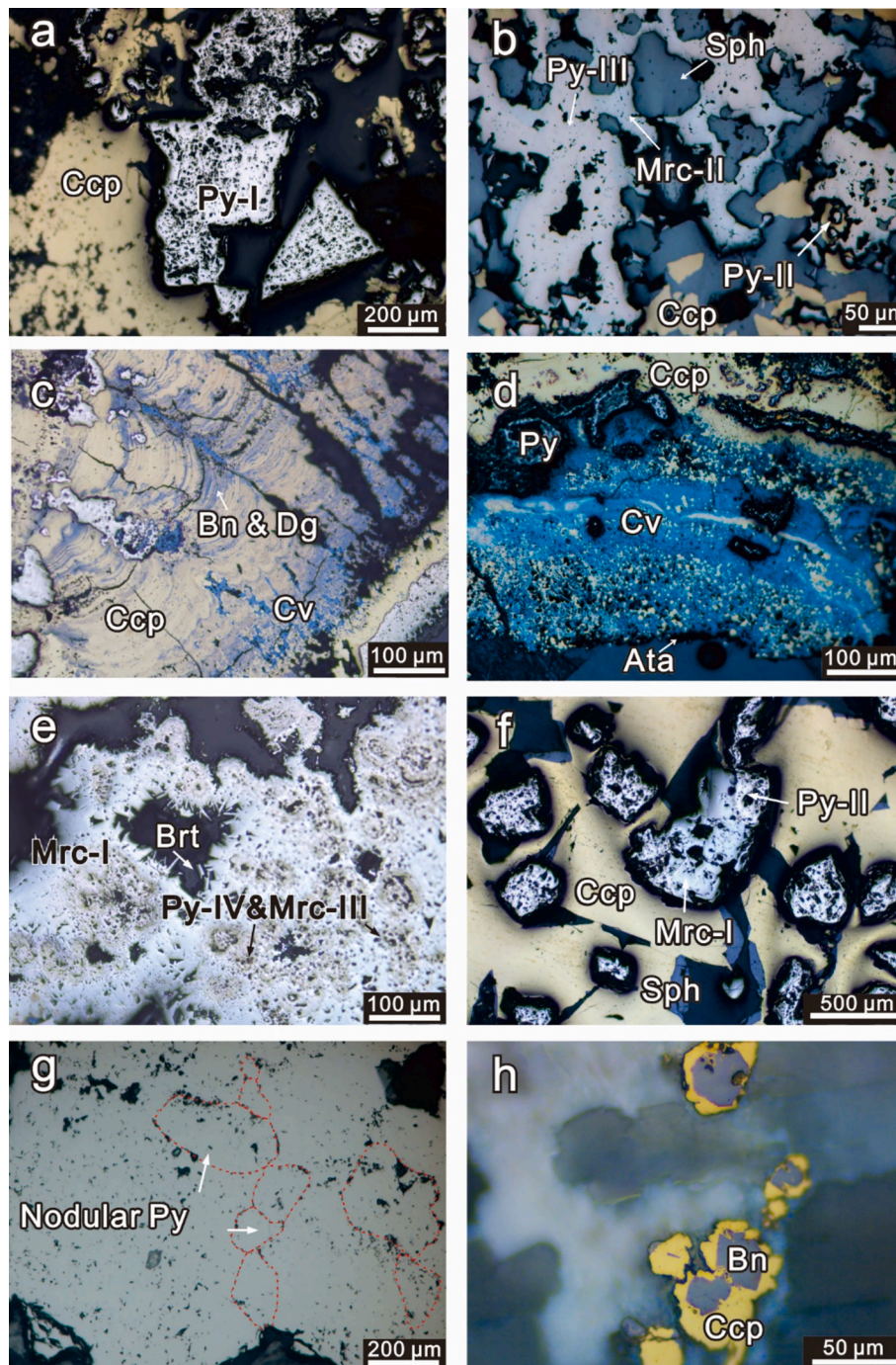
Fig. 4. Microscopic features of selected samples of the Wocan-1 hydrothermal mound. Images a~f are from samples collected in the southern and the central area of mound (SMW, BSZ and MF); g and h are from samples collected in the northern area of mound (NMW and BF). **a** Euhedral pyrite (Py-I) overgrown by chalcopyrite (Ccp) in the Cu-rich sulfide sample (sample JL131-G01), which is associated with high temperature conditions. **b** Euhedral sphalerite and chalcopyrite are overgrown by late-formed subhedral marcasite (Mrc-II) and pyrite (Py-III) which are likely formed at intermediate temperatures (sample JL129-G01). **c** Chalcopyrite, bornite and digenite precipitated in colloform texture and replaced by covellite in the outer layer of organ pipe chimney (JL125-G09). **d** Chalcopyrite replaced by covellite and overgrown by atacamite at the surface of a Cu-rich chimney (sample JL131-G01). **e** Colloform pyrite and marcasite rimed by marcasite (Mrc-I), overgrowing the platy barite in the exterior wall of a Cu-rich chimney (sample JL131-G04). **f** Early-formed euhedral and subhedral pyrite grains (Py-II) overgrown by chalcopyrite in the core of a Cu-rich chimney (sample JL131-G04). **g** Nodular pyrite aggregates in the massive pyrite sample (sample JL131-G03). **h** Bornite overgrown by chalcopyrite in the pore space of anhydrite (sample JL125-G17). Images are reflected-light photomicrographs in plane-polarized light (RL-PPL).

accepted standard Balmat Ruttan pyrite, $\delta^{34}S_{V-CDT}$ values of 1.2 ‰ (Crowe and Vaughan 1996). Sample measurements were bracketed every three to four analyses by at least one standard measurement to ensure precision and to account for instrument drift. The spot-to-spot reproducibility (external precision) was typically better than ± 0.57 ‰ (2σ) for pyrite and marcasite.

4. Results

4.1. Ocean floor observation and geological mapping

Hydrothermal activity in Wocan-1 is associated with the intersection of ridge-parallel normal faults and lava domes. Basalt outcrops are
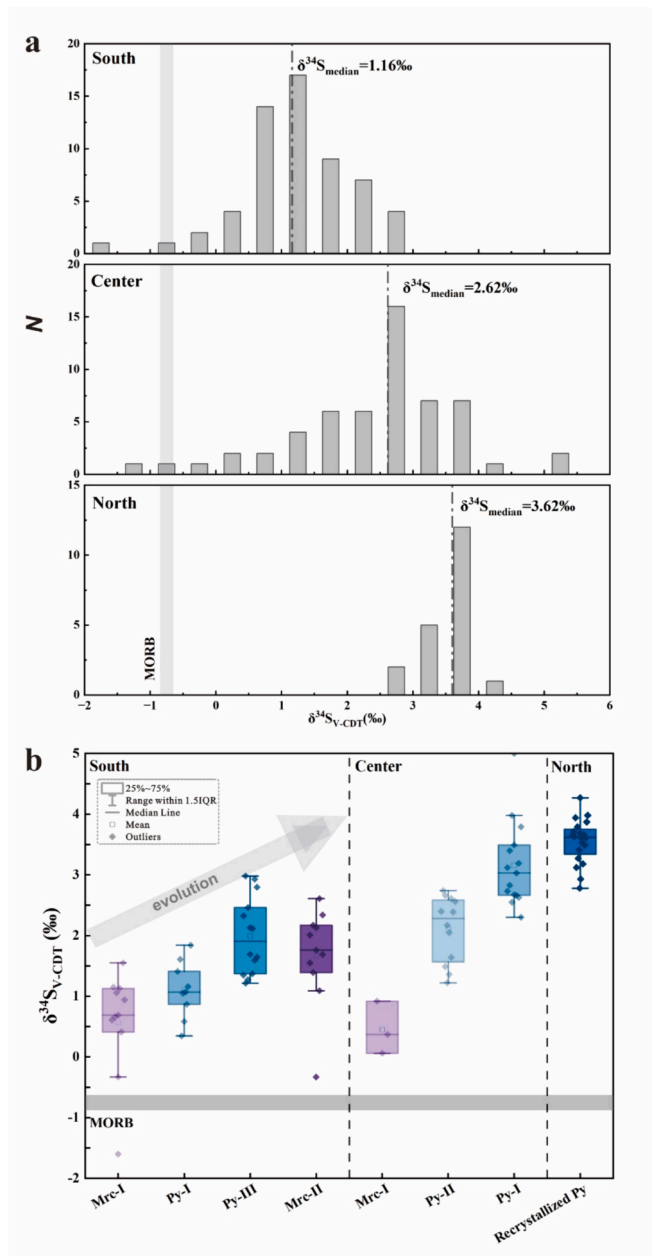
Fig. 5. Temporal and spatial differences of $\delta^{34}S_{V-CDT}$ values from Wocan-1 mound. **a** Frequency distribution of $\delta^{34}S_{V-CDT}$ values of pyrite and marcasite from southern (SMW & BSZ), central (MF) and the northern (NMW & BZ) areas of the mound. **b** Temporal difference of pyrite and marcasite $\delta^{34}S$ values from three areas of the mound. The median values are denoted as dashed lines and the sulfur isotope ratio of MORB ($\delta^{34}S=-0.9$ to -0.6 ‰, Labidi et al. 2012, 2014) as grey lines.

widely distributed around the mound (Fig. 1b), with basalt breccia, pillow basalts, sheet flows, and jumbled flows being observed. The mineral mound is ~ 260 m wide and ~ 50 m high (Fig. 1b).

There are three active vent sites known on this mound, located on the summit area and along the northern and eastern slopes of the mound, respectively (Fig. 1b). Each site shows distinct venting style and fluid temperature with different size and morphology of the chimneys (Table 1). The largest active vent site, the Black Smoker Zone (BSZ), is located near the summit and along the southeastern slope of the mound where steep cliffs commonly expose massive sulfides. There are 30 ~ 50 black smokers distributed as individual chimneys or complexes, which are 3 ~ 10 m high. A line of active chimneys runs from the base to the

top of the mound (Fig. 2a), while other active chimneys with 2 ~ 3 m tall, 0.2 ~ 0.5 m in diameter, forming clusters and vigorous venting black hydrothermal fluid with a maximum temperature of 358 °C (Qiu et al. 2021). The second area of active venting, Mulberry Forest (MF), occurs ~ 70 m northwest to the summit area, is located on a gentle slope, and consists of a dense group of chimneys resembling organ pipes. These chimneys, generally covered by Fe-oxihydroxides, are less than 2 m in height and 0.01 ~ 0.1 m in diameter. Most of the chimneys at this site are inactive with only a few active vents being present that currently vent clear fluids (Fig. 2b). An area with diffuse venting is observed adjacent to MF (Fig. 2c). Further north, in the Beehive Zone (BZ), chimneys with beehive structure were observed (<3m high), with the largest beehive being about 2 m tall and 1 m in diameter (Fig. 2d, e). Vigorous venting is rare throughout the BZ and adjacent areas (Fig. 1b) but shimmering water emitting from cracks is commonly observed. The measured temperatures of the fluids at the base of the small mound were up to 117 °C.

Extensive mass wasting was observed on the surface and along the margins of the Wocan-1 mound. The most significant mass wasting is documented at the northern margin of the mound (site NMW). The sulfide talus ranging in size from ~ 2 m to gravel-sized (Fig. 2f, g). The oxidized sulfide blocks extend up to ~ 50 m away from the mounds edge (Fig. 1b). Anhydrite sands are also commonly observed and covers an area of nearly 900 m^2 in the north (Fig. 1b). Further down slope, fine-grained metalliferous sediments extend for another ~ 200 m in flatter areas (Fig. 1b). On the southern slope, the mass wasting (site SMW) extends for 100 m from the summit of the mound to its base (Fig. 1b). Within the SMW area, sulfide blocks are commonly coated by greenish atacamite (Fig. 2h, 3b), a Cu-rich oxidation mineral common at hydro-thermal vents (Hannington, 1993).

4.2. Mineralogy

Samples from Wocan-1 mound can be classified into 1) Cu-rich sulfide chimneys, 2) Pyrite breccias and 3) Anhydrite-pyrite breccias (Fig. 3a ~ f). Cu-rich sulfide chimneys were collected from the central and southern vent sites (BSZ, SMW and MF), while pyrite breccias and anhydrite-pyrite breccias were mainly obtained from northern areas (BZ and NMW) (Table 2).

Cu-rich sulfide chimneys commonly exhibit fluid channels with mineral zonation from the inner conduit to the outer layer. The exterior wall is dominated by a mineral assemblage of marcasite, pyrite, and barite, while the middle and interior layer of the chimney walls is primarily composed of chalcopyrite, sphalerite, and pyrite (Fig. 3c and d). Some chimneys with particularly abundant copper sulfide are observed with a thin or absent pyrite and marcasite exterior layer (Fig. 3b and c). Instead, there is abundant and bornite, digenite, covellite and atacamite (Fig. 3b, 4c, 4d). The typical case is the organ-pipe chimney, in which the Cu-sulfide content exceeds 85 % (Fig. 3c). In these samples, chalcopyrite is the most abundant mineral, exhibiting a range of textures, including subhedral, euhedral, and massive, from the outer layer to the inner layer (Fig. 4a ~ d), while euhedral chalcopyrite has also been observed in the core of the chimney (Fig. 4f). The chalcopyrite-bornite-digenite in the exterior chimney wall are in intergrowth microlayers and overgrown by covellite, with the atacamite in the surface of the sample (Fig. 4c). Pyrite has four morphologically distinct generations. Pyrite-I in the euhedral texture, with is commonly overgrown by massive chalcopyrite or as aggregates and form a dense layer (Fig. 4a, 3d). Pyrite-II occurs in the subhedral texture precipitate with minor marcasite (Mrc-I) (Fig. 4f). Most of the pyrite-III were found to co-precipitate with marcasite (Mrc-II) and associated with sphalerite which precipitate later than the chalcopyrite (Fig. 4b). In some instances, the pyrite-III was observed to contain sphalerite inclusions, distributing along the growth layers. Colloform pyrite and marcasite microlayers are commonly occurs in the exterior wall. Sphalerite occurs as the rim of euhedral chalcopyrite and is usually in subhedral or anhedral texture (Fig. 4b). No major
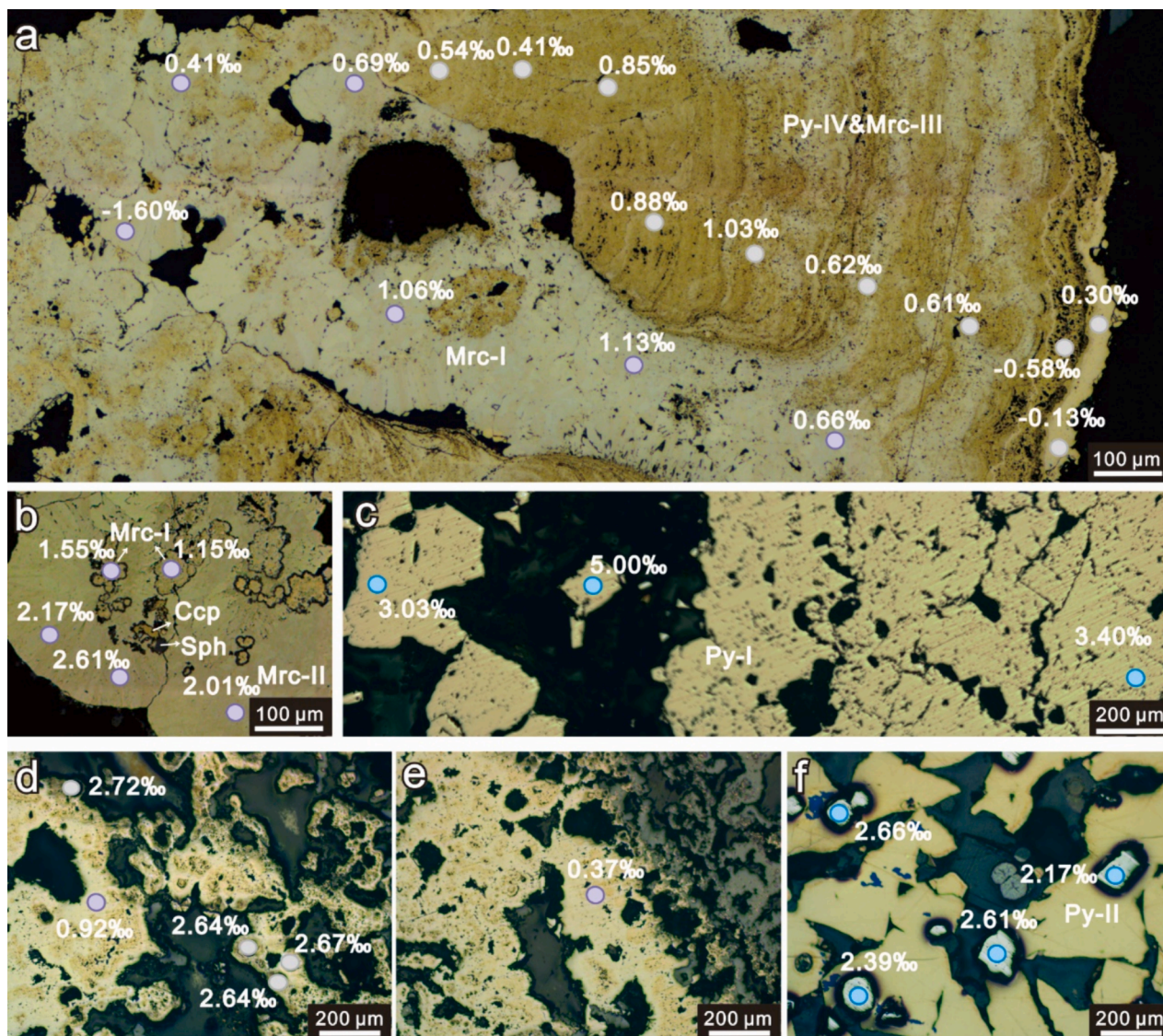
Fig. 6. δ^{34}S spot analysis location and δ^{34}S values of pyrite and marcasite. The samples were etched with NaOCl to reveal the detailed zonations. The colored spots showing the location of δ^{34}S analysis for marcasite (purple), pyrite (blue) and mixture of pyrite and marcasite (grey) respectively. Analyses are performed by Shrimp (a and b) and LA-MC-ICP-MS (c~f) respectively. **a** Colloform pyrite (Py-IV) and marcasite (Mrc-III) and subhedral marcasite (Mrc-I) (sample JL129-G01). **b** Marcasite (Mrc-II) with chalcopyrite, sphalerite and marcasite (Mrc-I) residual (sample JL129-G01). **c** Euhedral pyrite (Py-I) in the middle layer of a Cu-rich chimney (sample JL131-G04). **d, e** Colloform pyrite (Py-IV) and marcasite (Mrc-III) rimmed by subhedral marcasite (Mrc-I) in the exterior layer of a Cu-rich chimney (sample JL131-G04). **f** Subhedral pyrite (Py-II) overgrown by chalcopyrite in the core of a Cu-rich chimney (sample JL131-G04). (For interpretation of the references to colour in this figure legend, the reader is referred to the web version of this article.)

mineralogical differences are identified between southern and the central area of the mound, except for more marcasite, atacamite and less bornite were observed in the northern area.

Breccias are abundant in the northern margin of the mound, ranging in size from tens of centimeters to several meters. Pyrite breccias are primarily composed of pyrite, with the Fe-oxides present on the surface (Fig. 3e). Anhydrite-pyrite breccias are in matrix cemented structure and consist mainly of pyrite and anhydrite with minor chalcopyrite and bornite occurring in the anhydrite matrix (Fig. 3f). Both types of breccias are characterized by the presence of pyrite in nodular texture. The nodular pyrite occurs as aggregates or single pyrite grains with sizes varying from tens of micrometers to a few centimeters. Sequential overgrowth layers of pyrite and residual inclusions of chalcopyrite occasionally seen in the breccias. Fine chalcopyrite grains are present in the anhydrite matrix and some of these grains overgrow early-formed bornite (Fig. 4h).

4.3. Sulfur isotopic composition

We conducted in-situ sulfur isotope analysis on pyrite and marcasite in six sulfide samples. The complete 135 sulfur isotope data of sulfide minerals are given in Table A1. Overall, the δ^{34}S values of Wocan-1 mound range from $-1.60 \sim 5.04$ ‰ ($\delta^{34}S_{median} = 2.12$ ‰, n = 135).

Cu-rich chimneys from the southern vent sites (BSZ and SMW) have δ^{34}S values ranging from -1.60 to 2.98 ‰ with a median value of 1.16 ‰ (n = 59, Fig. 5a). The median δ^{34}S values of euhedral py-I, py-III and colloform py-IV/mrc-III are 1.07 ‰ (n = 9), 1.91 ‰ (n = 14) and 0.61 ‰ (n = 16) respectively, showing a relative ^{34}S enrichment in py-III (Fig. 5b) and a depletion in ^{34}S in pyrite/marcasite with colloform texture. The δ^{34}S values of colloform py-IV/mrc-III ranging from -0.58 to 1.34 ‰ do not seem to vary regularly from the exterior to the inside in samples from BSZ (Fig. 6a). In addition, the median values of subhedral mrc-I (early phase) and mrc-II (late phase) are 0.69 ‰ (n = 11) and 1.76 ‰ (n = 9) respectively. The median δ^{34}S values of late formed subhedral
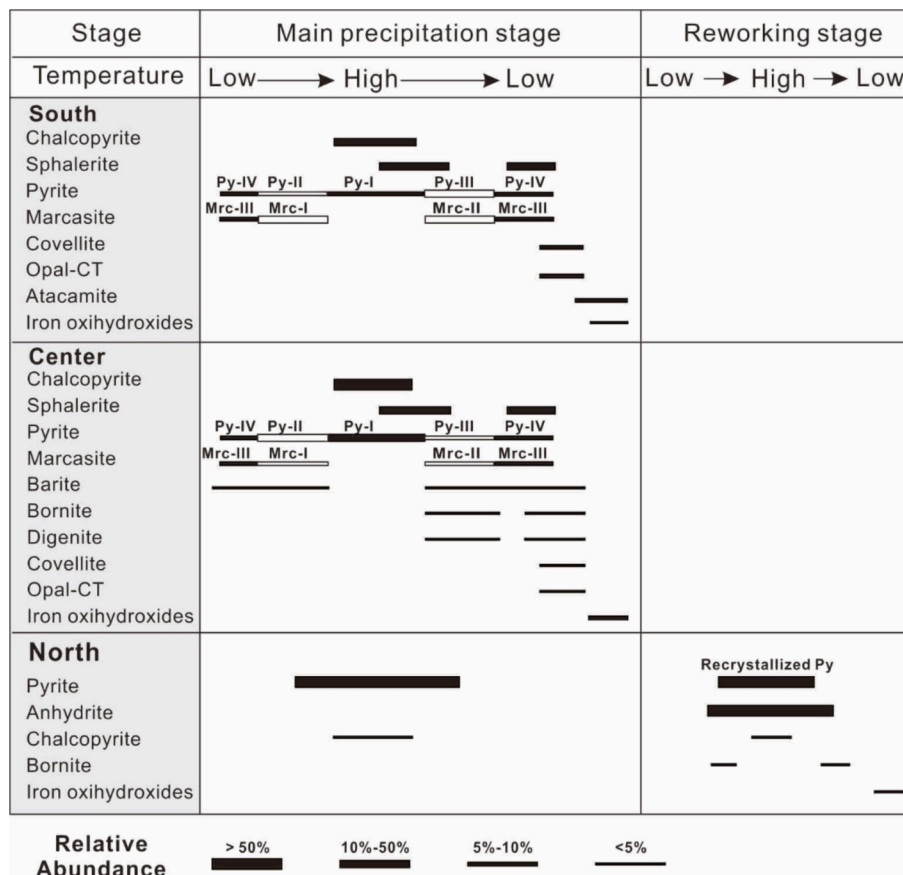
Fig. 7. Multiple stages of mineralization at Wocan-1 mound. The abundance and the paragenetic sequences of minerals are interpreted based on the samples and the seafloor observation at Wocan-1 mound.

mrc-II and py-III are similar (Fig. 5b). It is notable that negative $\delta^{34}S$ values have been observed in mrc-I, with the lowest $\delta^{34}S$ value of -1.60 ‰ (Fig. 6a).

Cu-rich chimneys from the central area of the mound (MF and its adjacent area) have $\delta^{34}S$ values ranging from -1.47 to 5.04 ‰, with a median value of 2.62 ‰ (n = 56, Fig. 5a). The layer of euhedral py-I has heavier $\delta^{34}S$ values ($\delta^{34}S_{median}$ = 3.03 ‰, n = 15) than subhedral py-II ($\delta^{34}S_{median}$ = 2.28 ‰, n = 12) in the interior layer (Fig. 6c and f). The $\delta^{34}S$ values of colloform py-IV/mrc-III in these samples cover a wide range, from $-1.47 \sim 5.04$ ‰, with a median value of 2.63 ‰ (n = 26).

Breccias from the northern vent sites (BF and NMW) shows a narrow range of $\delta^{34}S$ values of pyrite ranging from 2.78 to 4.27 ‰ with a median $\delta^{34}S$ value of 3.62 ‰ (n = 20, Fig. 5a). Pyrite in the BF and NMW sites are isotopically heavier by ~ 2 ‰ than that in the BSZ site.

5. Discussion

5.1. Spatial variation of mineralization

According to the geological mapping and the mineralogy analysis, there is significant difference in mineralization features between central-southern area and northern area (Fig. 7).

The southern and central part of the mound (BSZ, MF and SMW) are significantly enriched in copper-rich minerals (Fig. 2h, 3a ~ d), particularly chalcopyrite, suggesting the sustained influence of high-temperature hydrothermal activity (Hannington et al. 1995). The northern part of the mound (BZ and NMW) is primarily composed of pyrite and anhydrite (Fig. 2d ~ g, 3e and f). The absence of copper-rich materials indicates lower temperatures in this area. The abundance of anhydrite, often present as nodular pyrite-anhydrite breccias (Fig. 3f),

provides strong evidence of intense mixing of seawater and hydrothermal fluids in the subsurface of the mound (Lowell et al., 2003). The presence of such anhydrite precipitation and shallow mixing of hydrothermal fluids and seawater has been observed at the active TAG mound, where elongated collapse areas have been known to expose anhydrite (Humphris and Kleinrock 1996).

Based on these findings, it is considered that such a seawater ingress into the mound influence the spatial distribution of hydrothermal precipitates at Wocan-1 mound. This facilitates precipitation of high-temperature sulfides in the subseafloor, which can lead to the formation of barren Fe-rich sulfides at the margin.

5.2. Controls of mineralization and geological model

The different venting styles observed at Wocan-1 provide further insight into the mixing of hydrothermal fluids and seawater within the mound (Fig. 2a ~ d). Currently, high-temperature black smokers are mainly venting near the summit of the mound, emitting dense clouds of black smoke (BSZ; Fig. 2a). This indicates limited subseafloor mixing of ascending hydrothermal fluids and seawater at this site, resulting in a significant loss of metals to the seawater. In contrast to the venting at the summit, the venting in the central area (MF) and in the north (BZ) is clear and free of metal-rich black smoke (Fig. 2b ~ d). This suggests that metal precipitation occurred prior to venting and that sulfide has accumulated within the mound or further beneath the seafloor (Hannington et al. 1995). The dense distribution of inactive organ pipe chimneys with iron-oxyhydroxides on their surface reveals an intense hydrothermal activity in the central area in the past (Fig. 2b). The overall lower flux in the central region when compared to the summit could be due to the clogging of fluid channels caused by metal
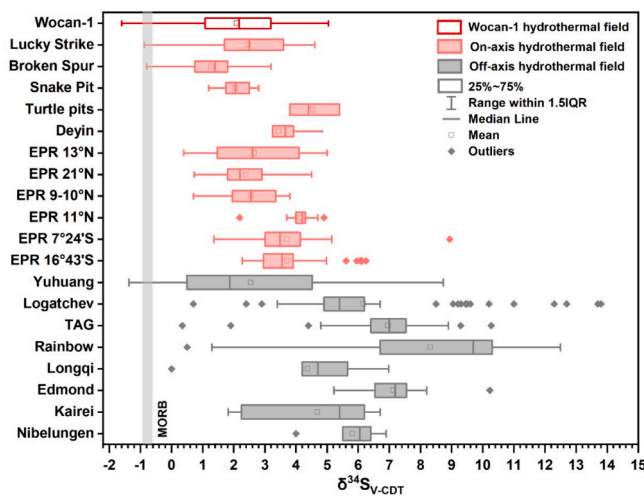
Fig. 8. Sulfur isotope values of sulfides samples from hydrothermal fields in mid-ocean ridge. Data are from: Wocan-1 (this study); Lucky Strike (Ono et al. 2007; Rouxel et al., 2004a,b); Broken Spur (Duckworth et al. 1995; Butler et al. 1998); Snake Pit (Stuart et al. 1994; Kase et al. 1990); Turtle Pit (Peters et al. 2010); Deyin (Wang et al. 2020); EPR 13°N (Bluth and Ohmoto 1988; Ono et al. 2007; Zeng et al. 2017; Stuart et al. 1995; Zeng et al. 2010); EPR 21°N (Arnold and Sheppard, 1981; Kerridge et al. 1983; Woodruff and Shanks, 1988; Stuart et al. 1994; Hekinian et al. 1980; Zierenberg et al. 1984); EPR 9-10°N (Ono et al. 2007; Rouxel et al. 2008); EPR 11°N (Bluth and Ohmoto, 1988; Zeng et al. 2017); EPR 7°24'S (Marchig et al. 1997); EPR 16°43'S (Marchig et al. 1997); Yuhuang (Liao et al. 2018); Logatchev (Peters et al. 2010; Rouxel et al. 2004a; Zeng et al. 2017; Bogdanov et al. 1997); TAG (Chiba et al. 1998; Gemmell and Sharpe, 1998; Herzig et al. 1998; Knott et al., 1998; Stuart et al. 1994); Rainbow (Rouxel et al. 2004a; Lein et al. 2001; Bogdanov et al. 2002); Longqi (Zeng et al. 2017); Edmond (Wu et al. 2018; Zeng et al. 2017); Kairei (Zeng et al. 2017); Nibelungen (Peters et al. 2010). The sulfur isotope ratio of MORB (δ^{34}S=−0.9 to −0.6 ‰, Labidi et al. 2012, 2014) is shown as grey line.

precipitation in this area. In the northern areas, the diffuse venting is pervasive which is typical of a highly permeable substrate (Fouquet et al. 1993; Duckworth et al. 1995; Von Damm 2000; Lowell et al. 2003; Haase et al. 2007). This could, in this case, be related to the accumulation of sulfide debris in the northern areas. In addition, the normal faults, extending from the basaltic seafloor in the north into the mound (Fig. 1b) is considered to be another significant contributor to a high subseafloor permeability in this area. Together, these two factors could permit the formation of a secondary, shallow seawater circulation cell.

To better understand the process of seawater and hydrothermal fluid mixing and the contribution of seawater, we conducted further studies using sulfur isotope data. The δ^{34}S values of sulfide samples from the Wocan-1 mound range between −1.60 ~ 5.04 ‰, which is in agreement with previously published δ^{34}S values reported for sulfides in hydrothermal sediments (3.0 ~ 3.6 ‰; Popoola et al. 2019) and bulk analyses of massive sulfides (2.44 ~ 4.35 ‰; Wang et al., 2021b) from the Wocan-1 area. At sediment-starved mid-ocean ridges, sulfur is mainly derived from basalts (δ^{34}S = −0.9 to −0.6 ‰, Labidi et al. 2012, 2014) and seawater sulfates (δ^{34}S=21.24 ‰, Tostevin et al. 2014). Colloform pyrite and marcasite with negative sulfur isotope values are typically associated with microbial activity, which have been reported for sulfide samples from, for instance, Lucky Strike, the middle Okinawa Trough, and many others (Rouxel et al., 2004b; Nozaki et al. 2020). In addition, the light and negative values of Wocan-1 could also be attributed to sulfur derived from magmatic degassing (Herzig et al. 1998; de Ronde et al. 2011; Fan et al., 2021). Further studies are necessary to determine if Wocan-1 is similarly influenced.

The sulfur isotopic composition of pyrite and marcasite generations from different areas varies with the evolution of the hydrothermal fluid. The pyrite-III (δ^{34}S$_{median}$ = 1.91 ‰, n = 14) and marcasite-II (δ^{34}S$_{median}$ = 1.76 ‰, n = 9), formed at intermediate temperatures, show heavier δ^{34}S values than high temperature pyrite-I (δ^{34}S$_{median}$ = 1.07 ‰, n = 9) in the southern area of the mound (Fig. 5b). This suggests an increased contribution of seawater-derived sulfur in the system at intermediate temperatures. However, there is a contrast tendency presented by the chimney sample in the central area (δ^{34}S$_{py-I}$=3.03 ‰ > δ^{34}S$_{py-II}$=2.28 ‰; Fig. 5b, 6c-f) which can be explained by factors such as the temperature gradient or the residual time of seawater sulfate within the chimney wall (Wang et al., 2020; Meng et al., 2023). Higher temperature and longer residual time contribute to a heavier sulfur isotopic composition in the interior and dense layer of the chimneys (Fig. 6c-f). The recrystallized nodular pyrites associated with massive anhydrite in the north recorded relatively heavy sulfur isotope values. The range is narrow (δ^{34}S=2.78 to 4.27 ‰, median = 3.62 ‰, n = 20; Fig. 5b), which is considered to represent the δ^{34}S of a late-stage fluid responsible for recrystallization (Graham et al. 1988; Woodruff and Shanks 1988). The recrystallization process that is reworking existing mound sulfides (Fouquet et al. 1996) and involves an enhanced seawater contribution, will result in heavier δ^{34}S values during the ageing of the mound, a process that has not only been suggested for modern hydrothermal systems (e.g. Brother Volcano., de Ronde et al., 2019), but also for the Troodos VMS deposits (Martin et al. 2021). Large deposits, such as TAG, Yuhuang and Rainbow (German et al., 2016; Petersen et al., 2000; Yu
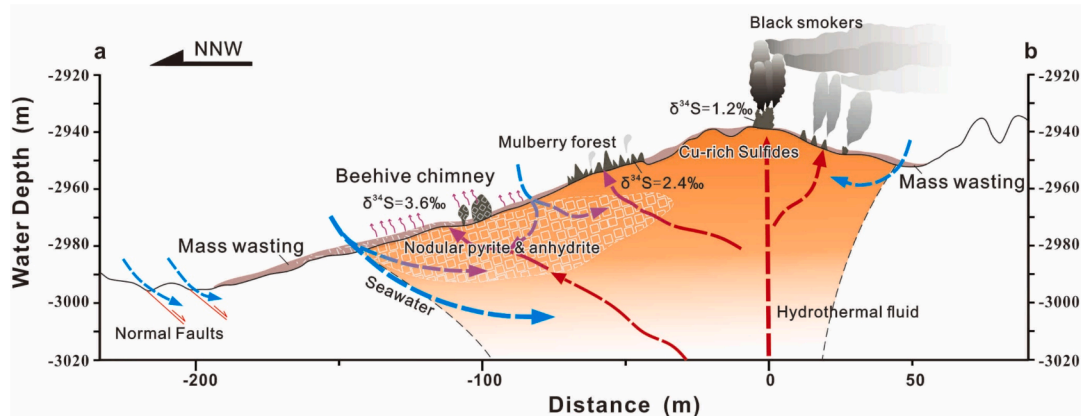
Fig. 9. Schematic model for the formation of Wocan-1 mineral mound. The location of the mound profile is shown in Fig. 1. Hydrothermal venting styles, mineralogy and sulfur isotopic composition is based on HOV observation and samples analysis. Red dashed lines indicate the ascending of hydrothermal fluid, and the blue dashed lines show the infiltration of seawater. (For interpretation of the references to colour in this figure legend, the reader is referred to the web version of this article.)

et al., 2021), exhibit wider ranges of sulfur isotopic composition compared to smaller deposits (Fig. 8). This further suggests a greater involvement of seawater during a potentially longer aging history.

The spatial $\delta^{34}S$ variation in Wocan-1 shows an overall increase from south to north, with median values of $\delta^{34}S_{south} = 1.16$ ‰, $\delta^{34}S_{center} = 2.62$ ‰, and $\delta^{34}S_{north} = 3.62$ ‰ (Fig. 5a). The contribution of seawater-derived sulfur increased by approximately 6 % and 11 % in the central and the northern areas, respectively, when compared to the southern sites, as calculated using a simple two-endmember mixing model (Ono et al. 2007). The enhanced seawater mixing could be caused by several processes. On one hand, the intense mass wasting and the accumulation of sulfide blocks during the formation of the northern part of the deposit provides highly permeable surfaces and a progressively larger space respectively, permitting more seawater to enter the mound and mix with hydrothermal fluids when compared to the south. Secondly, the normal faults, extending into the northern part of the mound (Fig. 1b), will provide additional pathways for seawater ingress. Thus, it is possible that the variation of $\delta^{34}S$ in Wocan-1 is associated with these faults. Faulting, in this case related to graben formation, is well established to favor seawater infiltration (Fouquet et al. 1996) and has been suggested by Bluth and Ohmoto (1988) to explain the shift in $\delta^{34}S$ from 1.7 ‰ in the early stages to 5 ‰ in the most recent high-temperature stage of a black smoker chimney at 13°N on the East Pacific Rise.

Overall, the spatial differences of mineralization at Wocan-1 are mainly controlled by interaction of ascending fluids with variable amounts of seawater due to permeability differences within the mound related to local collapse, mass wasting, and faulting. The infiltration of seawater in the north could result in a possible high-temperature sulfides precipitation and facilitate the reworking of the primary precipitates (Fig. 9).

5.3. Implications for the sulfide mineralization on the slow-spreading AVRs

The Wocan-1 mound is notable for several features, particularly the abundance of sulfide (~260 m in mound diameter) and the indicated significant resource potential. Other characteristics, include extensive mass wasting, the presence of anhydrite and nodular-pyrite textures, and a wide range of sulfur isotopic compositions. These characteristics are similar to those described for the off-axis TAG active mound (Humphris et al. 1995). Additionally, similar features, such as extensive mass wasting at Beebe (Webber et al., 2015) and abundant sulfates at Loki's Castle field (Pedersen et al., 2010), have also been reported for sites on the AVR. Based on these comparisons, we hypothesize that such features of the Wocan-1 could be commonality of some large sulfide mounds. The intense seawater infiltration and complex mineralization history are suggested to be significant factors in the formation of these deposits.

The presence of anhydrite at the faulted seafloor and the relatively heavy sulfur isotopic composition in samples at the northern mound emphasize the importance of faulting at Wocan-1 (Fig. 1b). Faulting has also been observed in other fields with large mound. The distribution of TAG hydrothermal precipitates is determined by the crossing faults and fissure populations, as identified by Kleinrock and Humphris (1996) and Graber et al. (2020). Furthermore, two mounds at Loki's Castle are reported to be controlled by two semi-parallel normal faults, with black smokers on the tops of the mounds and a low-temperature area adjacent to the eastern mound (Lim et al., 2019; Sahlström et al., 2023). Thus, it is believed that the local tectonic controls have a significant impact on the features and distribution of hydrothermal precipitates.

More controls on the formation of the large hydrothermal mound on the AVR should be considered. Previous studies suggest that the reduced volcanic activity could maintain long-lived conduits on the AVR, which provide a possibility for the formation of the large deposit (Pedersen et al., 2010; German et al., 2016). In the future study, further studies using geophysics and a larger scale geological mapping are necessary for the mechanisms of magmatic and tectonic activity, and their relationship with mineralization on the AVRs at the slow-spreading ridges.

6. Conclusion

The Wocan-1 sulfide mound, located on the axial volcanic ridge (AVR) of the slow-spreading Carlsberg ridge, exhibits approximately 260 m in diameter and 50 m in height. Spatially, the southern area of the mound is characterized by high-temperature Cu-rich sulfide chimneys, while the northern area is characterized by moderate-temperature beehive chimneys and a talus of pyrite-anhydrite breccias and sands extending for > 200 m. Mineralogy and sulfur isotope studies showed that the median values of $\delta^{34}S$ increases from south to north ($\delta^{34}S_{south} = 1.16$ ‰ $< \delta^{34}S_{center} = 2.62$ ‰ $< \delta^{34}S_{north} = 3.62$ ‰) and the recrystallized nodular pyrites in the northern area recorded heavy sulfur isotope values within a narrow range ($\delta^{34}S$=2.78 to 4.27 ‰, n = 20). It is considered that the normal faults extending into the northern area of the mound and the associated mass wasting facilitated the infiltration of seawater, which is responsible for the regional difference of the mineralization. We conclude that the local tectonic controls the features and distribution of hydrothermal precipitates. This study contributes to the understanding of the formation and controls of large sulfide mounds on the AVRs at the slow-spreading ridges which provide indications for the future seafloor exploration.

CRediT authorship contribution statement

Yiyang Cai: Conceptualization, Investigation, Writing-original draft, Writing-review & editing. **Xiqiu Han:** Conceptualization, Investigation, Writing-review & editing, Supervision. **Sven Petersen:** Conceptualization, Writing-review & editing. **Yejian Wang:** Conceptualization, Investigation, Writing-review & editing. **Zhongyan Qiu:** Investigation, Writing-review & editing. **Ming Yang:** Writing-review & editing.

Declaration of competing interest

The authors declare that they have no known competing financial interests or personal relationships that could have appeared to influence the work reported in this paper.

Data availability

Data will be made available on request.

Acknowledgements

Appendix A. Supplementary data

Supplementary data to this article can be found online at https://doi.org/10.1016/j.oregeorev.2024.106180.

References

Arnold, M., Sheppard, S.M.F., 1981. East Pacific Rise at latitude 21°N: Isotopic composition and origin of the hydrothermal sulphur. Earth Planet. Sci. Lett. 56, 148–156. https://doi.org/10.1016/0012-821X(81)90122-9.

Bluth, G.J., Ohmoto, H., 1988. Sulfide-sulfate chimneys on the East Pacific Rise, 11° and 13°N latitudes; Part II, Sulfur isotopes. Can. Mineral. 26, 505–515.

Bogdanov, Y.A., Bortnikov, N.S., Vikent'ev, I.V., Gurvich, E.G., Sagalevich, A.M., 1997. A new type of modern mineral-forming system: black smokers of the hydrothermal field at 14°45′N latitude, Mid-Atlantic Ridge. Geol. Ore Depos 39, 68–90.

Bogdanov, Y.A., Bortnikov, N.S., Vikent'ev, I.V., Lein, A.Y., Gurvich, E.G., Sagalevich, A.M., Simonov, V.A., 2002. Mineralogical-geochemical peculiarities of hydrothermal sulfide ores and fluids in the Rainbow Field associated with serpentinites, Mid-Atlantic Ridge (36°14′N). Geol. Ore Depos 44, 444.

Butler, I.B., Fallick, A.E., Nesbitt, R.W., 1998. Mineralogy, sulphur isotope geochemistry and the development of sulphide structures at the Broken Spur hydrothermal vent site, 29°10′N, Mid-Atlantic Ridge. J. Geol. Soc. London 155, 773–785. https://doi.org/10.1144/gsjgs.155.5.0773.

Cherkashov, G., Kuznetsov, V., Kuksa, K., Tabuns, E., Maksimov, F., Bel'tenev, V., 2017. Sulfide geochronology along the Northern Equatorial Mid-Atlantic Ridge. Ore Geol. Rev. SI: Marine Mineral Deposits: New Resources for Base, Precious, and Critical Metals 87, 147–154. https://doi.org/10.1016/j.oregeorev.2016.10.015.

Chiba, H., Uchiyama, N., Teagle, D.A.H., 1998. Stable isotope of anhydrite and sulfide minerals at the TAG hydrothermal mound, mid-atlantic ridge, 26°N. In: Herzig, P.M., Humphris, S.E., Miller, D.J., Zierenberg, R.A. (ed) Proc ODP, 158, Scientific Results, College Station, TX, pp 85-90. https://doi.org/10.2973/odp.proc.sr.158.1998.

Crowe, D.E., Vaughan, R.G., 1996. Characterization and use of isotopically homogeneous standards for in situ laser microprobe analysis of $^{34}S/^{32}S$ ratios. Am. Mineral. 81, 187.

de Ronde, C.E.J., Massoth, G.J., Butterfield, D.A., Christenson, B.W., Ishibashi, J., Ditchburn, R.G., Hannington, M.D., Brathwaite, R.L., Lupton, J.E., Kamenetsky, V.S., Graham, I.J., Zellmer, G.F., Dziak, R.P., Embley, R.W., Dekov, V.M., Munnik, F., Lahr, J., Evans, L.J., Takai, K., 2011. Submarine hydrothermal activity and gold-rich mineralization at Brothers Volcano, Kermadec Arc, New Zealand. Miner. Deposita 46, 541–584. https://doi.org/10.1007/s00126-011-0345-8.

de Ronde, C.E.J., Humphris, S.E., Höfig, T.W., Reyes, A.G., the IODP Expedition 376 Scientists, 2019. Critical role of caldera collapse in the formation of seafloor mineralization: the case of Brothers Volcano. Geology 47, 762–766. https://doi.org/10.1130/G46047.1.

Du, S., Wu, Z., Han, X., Wang, Y., Li, H., Zhang, J., 2023. Near-bottom magnetic anomaly features and detachment fault morphology in Tianxiu Vent Field, Carlsberg Ridge, Northwest Indian Ocean. Journal of Marine Science and Engineering 11, 918. https://doi.org/10.3390/jmse11050918.

Duckworth, R.C., Knott, R., Fallick, A.E., Rickard, D., Murton, B.J., Dover, C.V., 1995. Mineralogy and sulphur isotope geochemistry of the Broken Spur sulphides, 29°N, Mid-Atlantic Ridge. In: Parson, L.M., Walker, C.L., Dixon, D.R. (Eds.), Hydrothermal Vents and Processes. Geological Society, London, UK, pp. 175–189.

Fan, L., Wang, G., Holzheid, A., Zoheir, B., Shi, X., 2021. Sulfur and copper isotopic composition of seafloor massive sulfides and fluid evolution in the 26°S hydrothermal field Southern mid-Atlantic Ridge. Mar. Geol. 435, 106436 https://doi.org/10.1016/j.margeo.2021.106436.

Fouquet, Y., Wafik, A., Cambon, P., Mevel, C., Meyer, G., Gente, P., 1993. Tectonic setting and mineralogical and geochemical zonation in the Snake Pit sulfide deposit (Mid-Atlantic Ridge at 23° N). Econ. Geol. 88, 2018–2036. https://doi.org/10.2113/gsecongeo.88.8.2018.

Fouquet, Y., Knott, R., Cambon, P., Fallick, A., Rickard, D., Desbruyeres, D., 1996. Formation of large sulfide mineral deposits along fast spreading ridges. Example from off-axial deposits at 12°43′N on the East Pacific Rise. Earth Planet. Sci. Lett. 144, 147–162. https://doi.org/10.1016/0012-821X(96)00142-2.

Fouquet, Y., Charlou, J.L., Ondreas, H., Knoery, J., Donval, J.P., Douville, E., Apprioual, R., Cambon, P., Pelle, H., Landure, J.Y., Normand, A., Ponzevera, E., German, C., Parson, L., Barriga, F., Costa, I., Relvas, J., Ribeiro, A., 1997. Discovery and first submersible investigations on the Rainbow hydrothermal field on the MAR (36°14′N). Chem. Geol. 184, 37–48.

Fu, J., Hu, Z., Zhang, W., Yang, L., Liu, Y., Li, M., Zong, K., Gao, S., Hu, S., 2016. In situ sulfur isotopes ($\delta^{34}S$ and $\delta^{33}S$) analyses in sulfides and elemental sulfur using high sensitivity cones combined with the addition of nitrogen by laser ablation MC-ICP-MS. Anal. Chim. Acta 911, 14–26. https://doi.org/10.1016/j.aca.2016.01.026.

Gemmell, J.B., Sharpe, R., 1998. Detailed sulfur-isotope investigation of the TAG hydrothermal mound and stockwork zone, 26°N, Mid-Atlantic Ridge. In: Herzig, P.M., Humphris, S.E., Miller, J. (Eds.), Proc ODP 158. Scientific Results, College Station, TX, pp. 71–84.

German, C.R., Petersen, S., Hannington, M.D., 2016. Hydrothermal exploration of mid-ocean ridges: Where might the largest sulfide deposits be forming? Chem. Geol. 420, 114–126. https://doi.org/10.1016/j.chemgeo.2015.11.006.

Graber, S., Petersen, S., Yeo, I., Szitkar, F., Klischies, M., Jamieson, J., Hannington, M.D., Rothenbeck, M., Wenzlaff, E., Augustin, N., Stobbs, I., 2020. Structural control, evolution, and accumulation rates of massive sulfides in the TAG hydrothermal field. Geochem. Geophy. Geosy. https://doi.org/10.1029/2020GC009185.

Graham, U.M., Bluth, G.J., Ohmoto, H., 1988. Sulfide-sulfate chimneys on the East Pacific Rise, 11° and 13°N latitudes. Part I mineralogy and paragenesis. Can. Mineral. 26, 487–504.

Haase, K.M., Petersen, S., Koschinsky, A., Seifert, R., Devey, C.W., Keir, R., Lackschewitz, K.S., Melchert, B., Perner, M., Schmale, O., Süling, J., Dubilier, N., Zielinski, F., Fretzdorff, S., Garbe-Schönberg, D., Westernströer, U., German, C.R., Shank, T.M., Yoerger, D., Giere, O., Kuever, J., Marbler, H., Mawick, J., Mertens, C., Stöber, U., Walter, M., Ostertag-Henning, C., Paulick, H., Peters, M., Strauss, H., Sander, S., Stecher, J., Warmuth, M., Weber, S., 2007. Young volcanism and related hydrothermal activity at 5°S on the slow-spreading southern Mid-Atlantic Ridge. Geochem, Geophy, Geosy 8, Q11002. https://doi.org/10.1029/2006GC001509.

Han, X., Wang, Y., Li, X., 2015. First ultramafic-hosted hydrothermal sulfide deposit discovered on the Carlsberg Ridge. Northwest Indian Ocean, Presented at the third InterRidge theoretical insitute.

Hannington, MD, 1993. The formation of atacamite during weathering of sulfides on the modern seafloor. Can Mineral 31, 945–956.

Hannington, MD, de Ronde, C, Petersen, S, 2005. Sea-Floor Tectonics and Submarine Hydrothermal Systems, in: Economic Geology 100th Anniversary Volume, pp. 111–141. https://doi.org/10.5382/AV100.06.

Hannington, M., Jamieson, J., Monecke, T., Petersen, S., Beaulieu, S., 2011. The abundance of seafloor massive sulfide deposits. Geology 39, 1155–1158. https://doi.org/10.1130/G32468.1.

Hannington, M.D., Jonasson, I.R., Herzig, P.M., Petersen, S., 1995. Physical and chemical processes of seafloor mineralization at Mid-Ocean Ridges. In: Humphris, S.E., Zierenberg, R.A., Mullineaux, L.S., Thomson, R.E. (Eds.), Seafloor Hydrothermal Systems: Physical, Chemical, Biological, and Geological Interactions. American Geophysical Union, Washington DC, pp. 115–157. https://doi.org/10.1029/GM091p0115.

Hannington, M.D., Petersen, S., Jamieson, J., 2023. Another look at marine minerals. SEG Discovery 134, 19–30. https://doi.org/10.5382/SEGnews.2023-134.fea-01.

Hekinian, R., Fevrier, M., Bischoff, J.L., Picot, P., Shanks, W.C., 1980. Sulfide deposits from the East Pacific Rise near 21°N. Science 207, 1433–1444. https://doi.org/10.1126/science.207.4438.1433.

Herzig, P.M., Hannington Jr, M.D., Aa,, 1998. Sulfur isotopic composition of hydrothermal precipitates from the Lau back-arc: implications for magmatic contributions to seafloor hydrothermal systems. Miner. Deposita 33, 226–237.

Hu, Z., Zhang, W., Liu, Y., Gao, S., Li, M., Zong, K., Chen, H., Hu, S., 2015. "Wave" signal-smoothing and mercury-removing device for laser ablation quadrupole and multiple collector ICPMS analysis: application to lead isotope analysis. Anal. Chem. 87, 1152–1157. https://doi.org/10.1021/ac503749k.

Humphris, S.E., Herzig, P.M., Miller, D.J., Alt, J.C., Becker, K., Brown, D., Brügmann, G., Chiba, H., Fouquet, Y., Gemmell, J.B., Guerin, G., Hannington, M.D., Holm, N.G., Honnorez, J.J., Iturrino, G.J., Knott, R., Ludwig, K., Nakamura, K., Petersen, S., Reysenbach, A.L., Rona, P.A., Smith, S., Sturz, A.A., Tivey, M.K., Zhao, X., 1995. The internal structure of an active sea-floor massive sulphide deposit. Nature 377, 713–716. https://doi.org/10.1038/377713a0.

Humphris, S.E., Kleinrock, M.C., 1996. Detailed morphology of the TAG active hydrothermal mound: Insights into its formation and growth. Geophys. Res. Lett. 23, 3443–3446. https://doi.org/10.1029/96GL03079.

Ireland, T.R., Schram, N., Holden, P., Lanc, P., Ávila, J., Armstrong, R., Amelin, Y., Latimore, A., Corrigan, D., Clement, S., Foster, J.J., Compston, W., 2014. Charge-mode electrometer measurements of S-isotopic compositions on SHRIMP-SI. Int. J. Mass Spectrom. 359, 26–37. https://doi.org/10.1016/j.ijms.2013.12.020.

Kase, K., Yamamoto, M., Shibata, T., 1990. Copper-rich sulfide deposit near 23°N, Mid-Atlantic Ridge: chemical composition, mineral chemistry, and sulfur isotopes. In: Proceedings of the Ocean Drilling Program, 106/109 Scientific Results. Ocean Drilling Program.

Kerridge, J.F., Haymon, R.M., Kastner, M., 1983. Sulfur isotope systematics at the 21°N site, East Pacific Rise. Earth Planet. Sci. Lett. 66, 91–100. https://doi.org/10.1016/0012-821X(83)90128-0.

Kleinrock, M.C., Humphris, S.E., 1996. Structural control on seafloor hydrothermal activity at the TAG active mound. Nature 382, 149–153. https://doi.org/10.1038/382149a0.

Knott, R, Fouquet, Y, Honnorez, J, Bohn, M, 1998. Petrology of hydrothermal mineralization: a vertical section through the TAG mound. Proceedings of the Ocean Drilling Program: Scientific Results 158, 5–26. In: https://doi.org/10.2973/odp.proc.sr.158.201.1998.

Labidi, J., Cartigny, P., Birck, J.L., Assayag, N., Bourrand, J.J., 2012. Determination of multiple sulfur isotopes in glasses: a reappraisal of the MORB δ34S. Chem. Geol. 334, 189–198.

Labidi, J., Cartigny, P., Hamelin, C., Moreira, M., Dosso, L., 2014. Sulfur isotope budget (^{32}S, ^{33}S, ^{34}S and ^{36}S) in Pacific-Antarctic Ridge basalts: a record of mantle source heterogeneity and hydrothermal sulfide assimilation. Geochim. Cosmochim. Acta 133, 47–67.

Lein, A., Ulyanova, N.V., Ulyanov, A.A., Cherkashev, G.A., Stepanova, T.V., 2001. Mineralogy and geochemistry of sulfide ores in ocean-floor hydrothermal fields associated with serpentinite protrusions. Russ. J. Earth Sci. 3, 371–393. https://doi.org/10.2205/2001ES000068.

Liao, S., Tao, C., Li, H., Barriga, F.J.A.S., Liang, J., Yang, W., Yu, J., Zhu, C., 2018. Bulk geochemistry, sulfur isotope characteristics of the Yuhuang-1 hydrothermal field on the ultraslow-spreading Southwest Indian Ridge. Ore Geol. Rev. 96, 13–27. https://doi.org/10.1016/j.oregeorev.2018.04.007.

Lim, A., Brönner, M., Johansen, S.E., Dumais, M., 2019. Hydrothermal activity at the ultraslow-spreading Mohns Ridge: new insights from near-seafloor magnetics. Geochem. Geophys. Geosyst. 20, 5691–5709. https://doi.org/10.1029/2019GC008439.

Lowell, R., Yao, Y., Germanovich, L., 2003. Anhydrite precipitation and the relationship between focused and diffuse flow in seafloor hydrothermal systems. J. Geophys. Res. 108 https://doi.org/10.1029/2002JB002371.

Marchig, V., Blum, N., Roonwal, G., 1997. Massive sulfide chimneys from the east pacific rise at 7°24′S and 16°43′S. Mar Georesour Geotec 15, 49–66. https://doi.org/10.1080/10641199709379934.

Martin, A.J., McDonald, I., Jenkin, G.R.T., McFall, K.A., Boyce, A.J., Jamieson, J.W., MacLeod, C.J., 2021. A missing link between ancient and active mafic-hosted seafloor hydrothermal systems – magmatic volatile influx in the exceptionally preserved Mala VMS deposit, Troodos. Cyprus. Chem Geol 567, 120127. https://doi.org/10.1016/j.chemgeo.2021.120127.

Meng, X., Li, X., Holzheid, A., Zoheir, B., Jin, X., Li, Z., Wang, H., Zhu, Z., Li, J., Zhao, J., Chu, F., 2023. Sulfur isotopes as a new indicator for the maturation of sulfide chimneys in submarine hydrothermal systems. Mar. Geol. 107191 https://doi.org/10.1016/j.margeo.2023.107191.

Nozaki, T., Nagase, T., Ushikubo, T., Shimizu, K., Ishibashi, J., D/V Chikyu Expedition 909 Scientists, 2020. Microbial sulfate reduction plays an important role at the initial stage of subseafloor sulfide mineralization. Geology 49, 222–227. https://doi.org/10.1130/G47943.1.

Ono, S., Shanks, W.C., Rouxel, O.J., Rumble, D., 2007. S-33 constraints on the seawater sulfate contribution in modern seafloor hydrothermal vent sulfides. Geochim. Cosmochim. Acta 71, 1170–1182. https://doi.org/10.1016/j.gca.2006.11.017.

Pedersen, R.B., Rapp, H.T., Thorseth, I.H., Lilley, M.D., Barriga, F.J.A.S., Baumberger, T., Flesland, K., Fonseca, R., Früh-Green, G.L., Jorgensen, S.L., 2010. Discovery of a black smoker vent field and vent fauna at the Arctic Mid-Ocean Ridge. Nat. Commun. 1, 126. https://doi.org/10.1038/ncomms1124.

Pelleter, E., Fouquet, Y., Etoubleau, J., Cheron, S., Labanieh, S., Josso, P., Bollinger, C., Langlade, J., 2017. Ni-Cu-Co-rich hydrothermal manganese mineralization in the Wallis and Futuna back-arc environment (SW Pacific). Ore Geol Rev, SI: Marine Mineral Deposits: New Resources for Base, Precious, and Critical Metals 87, 126–146. https://doi.org/10.1016/j.oregeorev.2016.09.014.

Peters, M., Strauss, H., Farquhar, J., Ockert, C., Eickmann, B., Jost, C.L., 2010. Sulfur cycling at the Mid-Atlantic Ridge: a multiple sulfur isotope approach. Chem. Geol. 269, 180–196. https://doi.org/10.1016/j.chemgeo.2009.09.016.

Petersen, S., Herzig, P.M., Hannington, M.D., 2000. Third dimension of a presently forming VMS deposit: TAG hydrothermal mound, Mid-Atlantic Ridge, 26°N. Miner. Deposita 35, 233–259. https://doi.org/10.1007/s001260050018.

Popoola, S., Han, X., Wang, Y., Qiu, Z., Ye, Y., Cai, Y., 2019. Mineralogical and geochemical signatures of metalliferous sediments in Wocan-1 and Wocan-2 hydrothermal sites on the Carlsberg Ridge, Indian Ocean. Minerals 9, 1–19. https://doi.org/10.3390/min9010026.

Qiu, Z., Han, X., Li, M., Wang, Y., Chen, X., Fan, W., Zhou, Y., Cui, R., Wang, L., 2021. The temporal variability of hydrothermal activity of Wocan hydrothermal field, Carlsberg Ridge, northwest Indian Ocean. Ore Geol. Rev. 132, 103999 https://doi.org/10.1016/j.oregeorev.2021.103999.

Raju, K.A., Chaubey, A.K., Amarnath, D., Mudholkar, A., 2008. Morphotectonics of the Carlsberg Ridge between 62°20′ and 66°20′E, northwest Indian Ocean. Mar. Geol. 252, 120–128. https://doi.org/10.1016/j.margeo.2008.03.016.

Rona, P.A., Klinkhammer, G., Nelsen, T.A., Trefry, J.H., Elderfield, H., 1986. Black smokers, massive sulphides and vent biota at the Mid-Atlantic Ridge. Nature 321, 33–37. https://doi.org/10.1038/321033a0.

Rouxel, O., Fouquet, Y., Ludden, J.N., 2004a. Copper isotope systematics of the Lucky Strike, Rainbow, and Logatchev sea-floor hydrothermal fields on the Mid-Atlantic Ridge. Econ. Geol. 99, 585–600. https://doi.org/10.2113/gsecongeo.99.3.585.

Rouxel, O., Fouquet, Y., Ludden, J.N., 2004b. Subsurface processes at the Lucky Strike hydrothermal field, Mid-Atlantic Ridge: evidence from sulfur, selenium, and iron isotopes. Geochim. Cosmochim. Acta 68, 2295–2311. https://doi.org/10.1016/j.gca.2003.11.029.

Rouxel, O., Shanks, W., Bach, W., Edwards, K., 2008. Integrated Fe- and S-isotope study of seafloor hydrothermal vents at East Pacific Rise 9–10°N. Chem. Geol. 252, 214–227. https://doi.org/10.1016/j.chemgeo.2008.03.009.

Sahlström, F., Strmić Palinkaš, S., Hjorth Dundas, S., Sendula, E., Cheng, Y., Wold, M., Pedersen, R.B., 2023. Mineralogical distribution and genetic aspects of cobalt at the active Fåvne and Loki's Castle seafloor massive sulfide deposits Arctic mid-Ocean Ridges. Ore Geol. Rev. 153, 105261.

Stuart, F.M., Turner, G., Duckworth, R.C., Fallick, A.E., 1994. Helium isotopes as tracers of trapped hydrothermal fluids in ocean-floor sulfides. Geology 22, 823–826. https://doi.org/10.1130/0091-7613(1994)022<0823:HIATOT>2.3.CO;2.

Stuart, F.M., Harrop, P.J., Knott, R., Fallick, A.E., Turner, G., Fouquet, Y., Rickard, D., 1995. Noble gas isotopes in 25 000 years of hydrothermal fluids from 13°N on the East Pacific Rise. Geol. Soc. Lond. Spec. Publ. 87, 133–143. https://doi.org/10.1144/GSL.SP.1995.087.01.12.

Tao, C., Li, H., Huang, W., Han, X., Wu, G., Su, X., Zhou, N., Lin, J., He, Y., Zhou, J., 2011. Mineralogical and geochemical features of sulfide chimneys from the 49°39′E hydrothermal field on the Southwest Indian Ridge and their geological inferences. Sci. Bull. 56, 2828–2838.

Teagle, D.A.H., Alt, J.C., 2004. Hydrothermal alteration of basalts beneath the bent hill massive sulfide deposit, Middle Valley, Juan de Fuca Ridge. Econ. Geol. 99, 561–584. https://doi.org/10.2113/99.3.561.

Tostevin, R., Turchyn, A.V., Farquhar, J., Johnston, D.T., Eldridge, D.L., Bishop, J.K.B., McIlvin, M., 2014. Multiple sulfur isotope constraints on the modern sulfur cycle. Earth Planet. Sci. Lett. 396, 14–21.

Von Damm, K.L., 2000. Chemistry of hydrothermal vent fluids from 9°-10°N, East Pacific Rise: "Time zero", the immediate posteruptive period. J. Geophys. Res. 105, 11203–11222. https://doi.org/10.1029/1999JB900414.

Wang, Y., Han, X., Petersen, S., Frische, M., Qiu, Z., Li, H., Li, H., Wu, Z., Cui, R., 2017. Mineralogy and trace element geochemistry of sulfide minerals from the Wocan hydrothermal field on the slow-spreading Carlsberg Ridge, Indian Ocean. Ore Geol. Rev. 84, 1–19. https://doi.org/10.1016/j.oregeorev.2016.12.020.

Wang, Y., Han, X., Zhou, Y., Qiu, Z., Yu, X., Petersen, S., Li, H., Yang, M., Chen, Y., Liu, J., Wu, X., Luo, H., 2021b. The Daxi Vent Field: an active mafic-hosted hydrothermal system at a non-transform offset on the slow-spreading Carlsberg Ridge, 6°48′N. Ore Geol. Rev. 129, 103888 https://doi.org/10.1016/j.oregeorev.2020.103888.

Wang, S., Li, H., Zhai, S., Yu, Z., Shao, Z., Cai, Z., 2016. Mineralogical characteristics of polymetallic sulfides from the Deyin-1 hydrothermal field near 15°S, southern Mid-Atlantic Ridge. Acta Oceanol. Sin. 36, 22–34. https://doi.org/10.1007/s13131-016-0961-3.

Wang, S., Sun, W., Huang, J., Zhai, S., Li, H., 2020. Coupled Fe–S isotope composition of sulfide chimneys dominated by temperature heterogeneity in seafloor hydrothermal systems. Sci. Bull. 65, 1767–1774. https://doi.org/10.1016/j.scib.2020.06.017.

Wang, S., Sun, W., Huang, J., Zhai, S., 2021a. Iron and sulfur isotopes of sulfides from the Wocan hydrothermal field, on the Carlsberg Ridge Indian Ocean. Ore Geol. Rev. 133, 103971 https://doi.org/10.1016/j.oregeorev.2020.103971.

Wang, S., Li, C., Li, B., Dang, Y., Ye, J., Zhu, Z., Zhang, L., Shi, X., 2022. Constraints on fluid evolution and growth processes of black smoker chimneys by pyrite geochemistry: a case study of the Tongguan hydrothermal field South mid-Atlantic Ridge. Ore Geol. Rev. 140, 104410 https://doi.org/10.1016/j.oregeorev.2021.104410.

Webber, A.P., Roberts, S., Murton, B.J., Hodgkinson, M.R.S., 2015. Geology, sulfide geochemistry and supercritical venting at the Beebe Hydrothermal Vent Field, Cayman Trough. Geochem Geophy Geosy 16, 2661–2678. https://doi.org/10.1002/2015GC005879.

Woodruff, L.G., Shanks, W.C., 1988. Sulfur isotope study of chimney minerals and vent fluids from 21°N, East Pacific Rise: Hydrothermal sulfur sources and disequilibrium sulfate reduction. J. Geophys. Res. 93, 4562–4572. https://doi.org/10.1029/JB093iB05p04562.

Wu, Z., Sun, X., Xu, H., Konishi, H., Wang, Y., Lu, Y., Cao, K., Wang, C., Zhou, H., 2018. Microstructural characterization and in-situ sulfur isotopic analysis of silver-bearing sphalerite from the Edmond hydrothermal field, Central Indian Ridge. Ore Geol. Rev. 92, 318–347. https://doi.org/10.1016/j.oregeorev.2017.11.024.

Yu, X., Han, X., Qiu, Z., Wang, Y., Tang, L., 2019. Definition of Northwest Indian Ridge and its geologic and tectonic signatures. Earth Sci. 44, 626–639. https://doi.org/10.3799/dqkx.2018.136.

Yu, J., Tao, C., Liao, S., Alveirinho Dias, Á., Liang, J., Yang, W., Zhu, C., 2021. Resource estimation of the sulfide-rich deposits of the Yuhuang-1 hydrothermal field on the ultraslow-spreading Southwest Indian Ridge. Ore Geol. Rev. 134, 104169 https://doi.org/10.1016/j.oregeorev.2021.104169.

Zeng, Z., Chen, D., Yin, X., Wang, X., Zhang, G., Wang, X., 2010. Elemental and isotopic compositions of the hydrothermal sulfide on the East Pacific Rise near 13°N. Sci. China Earth Sci. 53, 253–266. https://doi.org/10.1007/s11430-010-0013-3.

Zeng, Z., Hu, P., He, Z., Yao, J., Yang, Z., 2024. Numerical simulation study of seafloor hydrothermal circulation based on hydrothermal foam: a case study of the Wocan-1 hydrothermal field, Carlsberg Ridge Indian Ocean. J. Mar. Sci. Eng. 12, 46. https://doi.org/10.3390/jmse12010046.

Zeng, Z., Ma, Y., Chen, S., Selby, D., Wang, X., Yin, X., 2017. Sulfur and lead isotopic compositions of massive sulfides from deep-sea hydrothermal systems: implications for ore genesis and fluid circulation. Ore Geol. Rev. 87, 155–171. https://doi.org/10.1016/j.oregeorev.2016.10.014.

Zhang, T., Tang, J., Li, Z., Zhou, Y., Wang, X., 2018. Use of the *Jiaolong* manned submersible for accurate mapping of deep-sea topography and geomorphology. Sci. China Earth Sci. 61, 1148–1156. https://doi.org/10.1007/s11430-017-9187-3.

Zierenberg, R.A., Shanks, W.C., Bischoff, J.L., 1984. Massive sulfide deposits at 21°N, East Pacific Rise: Chemical composition, stable isotopes, and phase equilibria. Geol. Sco. Am. Bull. 95, 922–929. https://doi.org/10.1130/0016-7606(1984)95<922:MSDANE>2.0.CO;2.

Zong, T., Han, X., Liu, J., Wang, Y., Qiu, Z., Li, H., Yu, X., 2019. H$_2$O in basaltic glasses from the slow-spreading Carlsberg Ridge: implications for mantle source and magmatic processes. Lithos 332–333, 274–286. https://doi.org/10.1016/j.lithos.2019.01.022.